

# Site-specific symmetry sensitivity of angle-resolved photoemission spectroscopy in layered palladium diselenide

M. Cattelan

*Elettra Sincrotrone Trieste, SS 14, Km 163.5 AREA Sci. Pk., 34149 Trieste, Italy*

C. J. Sayers

*Dipartimento di Fisica, Politecnico di Milano, 20133 Milano, Italy*

D. Wolverson

*University of Bath, Ctr. Nanosci. and Nanotechnol., Dept. Phys., Bath BA2 7AY, UK*

E. Carpen<sup>\*</sup>

*IFN-CNR, Dipartimento di Fisica, Politecnico di Milano, 20133 Milano, Italy*

## Abstract

Two-dimensional (2D) materials with puckered layer morphology are promising candidates for next-generation opto-electronics devices owing to their anisotropic response to external perturbations and wide band gap tunability with the number of layers. Among them, PdSe<sub>2</sub> is an emerging 2D transition-metal dichalcogenide with band gap ranging from  $\sim 1.3$  eV in the monolayer to a predicted semimetallic behavior in the bulk. Here we use angle-resolved photoemission spectroscopy to explore the electronic band structure of PdSe<sub>2</sub> with energy and momentum resolution. Our measurements reveal the semiconducting nature of the bulk. Furthermore, constant binding-energy maps of reciprocal space display a remarkable site-specific sensitivity to the atomic arrangement and its symmetry. Supported by density functional theory calculations, we ascribe this effect to the inherent orbital character of the electronic band structure. These results not only provide a deeper understanding of the electronic configuration of PdSe<sub>2</sub>, but also establish additional capabilities of photoemission spectroscopy.

---

\*Electronic address: [ettore.carpen@polimi.it](mailto:ettore.carpen@polimi.it)

Transition metal dichalcogenides (TMDs) host highly attractive properties for fundamental studies of novel physical phenomena and for applications ranging from opto-electronics to sensing at the nanoscale [1, 2]. Among all TMDs, those based on noble metals (Pd, Pt) have received less attention because of their high cost, until the recent discovery of a layer-controllable metal-to-semiconductor transition [3–6], which motivated their investigation in the last few years. Similar to the extensively investigated black phosphorus [7–10], with a band gap varying from 0.3 eV in the bulk to 1.5 eV in the monolayer [11], PdSe<sub>2</sub> is characterized by an in-plane puckered structure resulting in an anisotropic response to external stimuli, such as light [12], electric field [13] and strain [14, 15]. In addition, a linear dependence of the band gap with the number of layers has been observed [3, 16]: the monolayer is predicted to have an indirect gap of 1.3 eV [17] which monotonically decreases to 0 eV as the thickness exceeds 40 – 50 layers, suggesting semimetallic behavior. However, unlike black phosphorous and the majority of TMDs which share hexagonal crystal structures, the low-symmetry pentagonal atomic arrangement of PdSe<sub>2</sub> gives rise to exotic thermoelectric, mechanical and optical properties [18–20].

Here, we investigate the electronic structure of PdSe<sub>2</sub> for the first time by angle-resolved photoemission spectroscopy (ARPES). We clarify the semiconducting nature of the bulk by direct measurements of the electronic bands in reciprocal space. Furthermore, we reveal a previously unexplored sensitivity of photoemission to the site-specific crystal symmetry. In particular, constant binding-energy cuts of the surface-projected Brillouin zone (BZ) disclose the dominant chemical/orbital character of the metal atoms on the top-most valence band, while the effect of the chalcogen species becomes relevant at binding energies exceeding 1 eV. This finding is corroborated by plane wave density functional theory (DFT) calculations employing Perdew-Burke-Ernzerhof (PBE) functional.

The crystallographic morphology of PdSe<sub>2</sub> is sketched in Fig.1. Its stable configuration is orthorhombic with Pbc<sub>a</sub> space group (#61) and experimental lattice parameters  $a = 0.575$  nm,  $b = 0.587$  nm and  $c = 0.77$  nm [21], see Fig.1a. Layers are normal to the  $c$ -axis. The top view (panel b) shows the characteristic pentagonal atomic arrangement of the monolayer, while the side view (panel c) reveals its puckered structure. Each PdSe<sub>2</sub> layer is formed by three atomic planes: Pd atoms in the middle are covalently bound to four Se atoms located on the top and bottom sub-layers. In contrast with other TMDs where the metal atom has +4 oxidation state, PdSe<sub>2</sub> adopts the +2 oxidation [22]. This is achieved

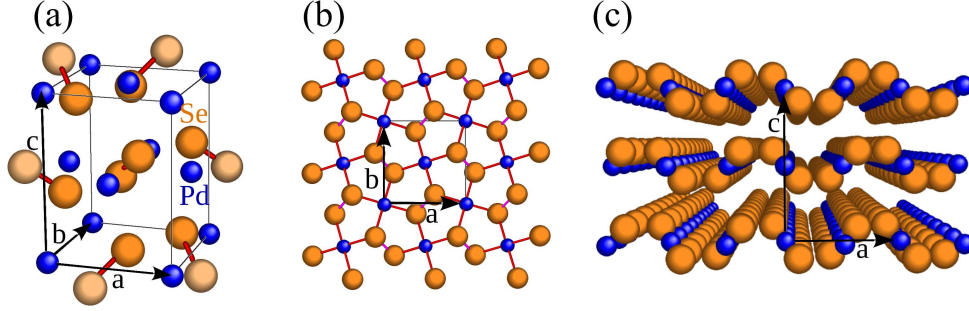


FIG. 1: Unit cell (a), top (b) and side (c) views of PdSe<sub>2</sub> crystal structure. The red links in panel (a) indicate the bonds related to Se<sub>2</sub> dimerization.

via (Se<sub>2</sub>)<sup>2-</sup> dimerization (see red links in Fig.1a) that provides further bonding between the top and the bottom chalcogen sub-layers.

Fig.2a shows the measured band structure of PdSe<sub>2</sub> along selected high symmetry directions, following the orthorhombic unit cell notation shown in the inset (see Methods for experimental details). The top of the valence band (VB) is located at the center of the BZ and is adjacent to the Fermi level  $E_F$ . The large spectral weight at the  $S$  point ( $E - E_F \simeq -3$  eV) suggests the intersection of several bands. Fig.2b reports the  $k$ -resolved

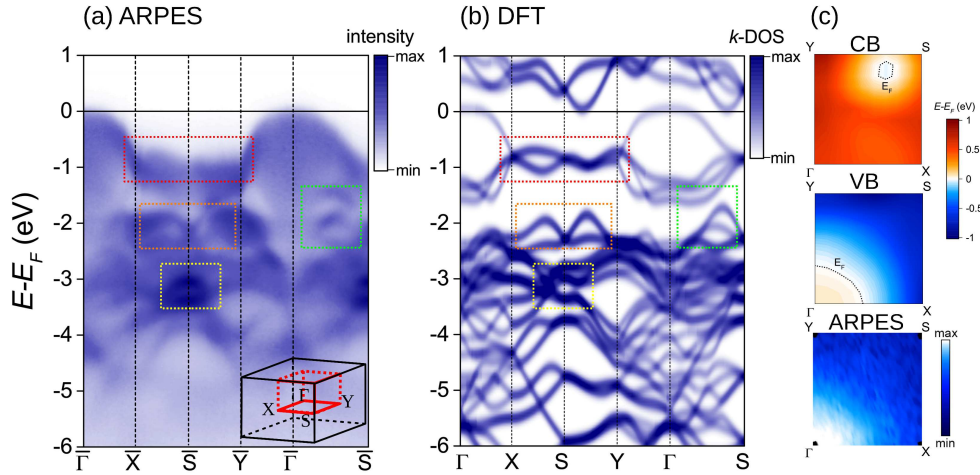


FIG. 2: (a) Electronic band structure of PdSe<sub>2</sub> measured by ARPES ( $h\nu = 74$  eV). The inset shows a sketch of the first BZ. (b)  $k$ -resolved DOS obtained with DFT calculations along the same path in reciprocal space used in panel a. (c) DFT mapping of the CB (top) and VB (middle) on a 2D portion of the first BZ: dashed black lines mark the Fermi level  $E_F$ . The 2D ARPES intensity map at  $E_F$  (bottom) reveals no signature of the CB.

density of states ( $k$ -DOS) obtained with DFT calculations along the same symmetry lines adopted in panel a (see Methods for computational details). The main features of the occupied states are reproduced with remarkable adherence to the experimental data, in particular the dispersion of the top VB and the large DOS at the  $S$  point and  $E - E_F \simeq -3$  eV, that in fact hosts an intricate overlap of several electronic bands. The coloured rectangles in panels a and b highlight additional features common to both measured and calculated band structures. Our DFT analysis identifies PdSe<sub>2</sub> as a semimetal: the top graph in Fig.2c shows the false-colour energy landscape of the lowest conduction band (CB) on a 2D portion of the BZ. The minimum is located close to the  $YS$  line (internal coordinates  $[k_x, k_y] \simeq [0.33, 0.43]$  at energy  $E - E_F \simeq -25$  meV). The middle graph shows the energy landscape of the highest VB, where its maximum occurs at the  $\Gamma$  point and energy  $E - E_F \simeq +55$  meV. Hence, there is an overall negative gap of approximately 80 meV. In contrast to the calculations, no evidence of electron pockets due to the CB crossing the Fermi level has been observed experimentally, as shown in the lowest graph of Fig.2c that reports the surface-projected ARPES map at the Fermi level. Thus, we conclude that PdSe<sub>2</sub> is most likely a semiconductor in the bulk (See Methods - Fig.5 - for additional evidence). This result is in agreement with recent optical measurements [23, 24], but diverges from calculations that predict semimetallic behaviour [3, 17, 25, 26]. While it is known that DFT generally underestimates band gaps in semiconductors [27, 28], the fact that VB and CB are well separated in reciprocal space preserves their individual electronic features, regardless of the computed value of the band gap. In particular, the occupied states (experimentally observed by ARPES) are reproduced by DFT with remarkable accuracy.

More insight on the electronic structure of PdSe<sub>2</sub> is achieved by inspecting the ARPES isoenergetic maps. Fig.3a shows the photoemission spectral weight measured on the reciprocal plane at constant energy  $E - E_F = -2.3$  eV (in Fig.3b it corresponds to the red horizontal line cutting the band structure). Horizontal and vertical axes are expressed in units of  $\pi/a$  and  $\pi/b$ , respectively. The red dashed lines identify the edges of the orthorhombic BZ. The spectral weight clearly resembles the symmetry of the BZ with peaks (yellow colour) at  $\bar{X}$  and  $\bar{Y}$  points and valleys (blue colour) at  $\bar{\Gamma}$ . For clarity, each  $\bar{\Gamma}$  point has been labeled with the corresponding in-plane Miller indices ( $hk$ ). Fig.3c shows a photoemission map at  $E - E_F = -0.4$  eV, i.e. closer to  $E_F$  (in Fig.3b, it corresponds to the blue horizontal line cutting the band structure). The observed elliptical shapes are the surface-projected

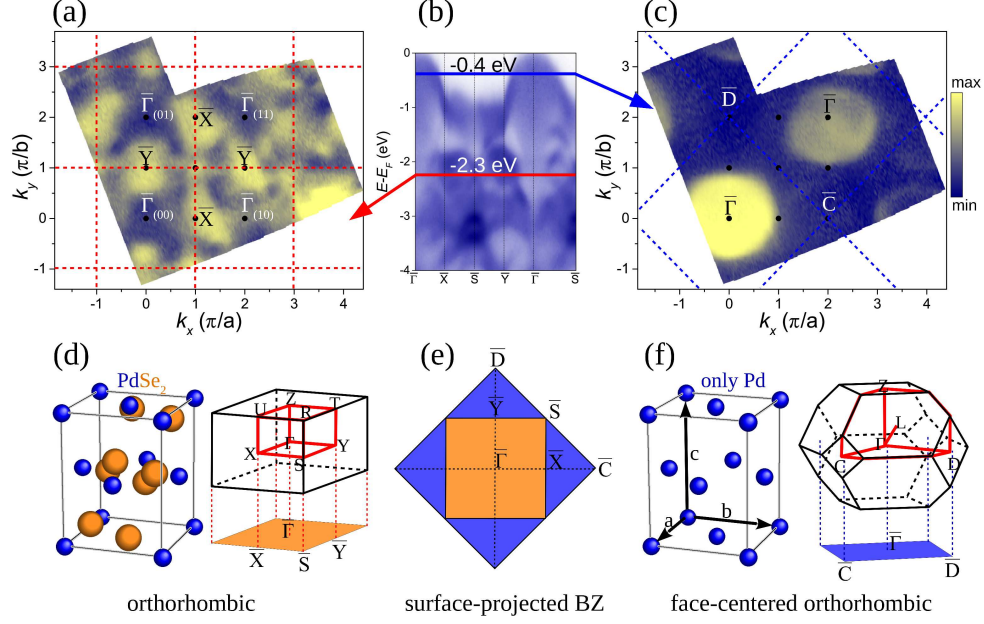


FIG. 3: Constant binding-energy ARPES maps at (a)  $E - E_F = -2.3$  eV and (c)  $E - E_F = -0.4$  eV. Red and blue dashed lines correspond to the surface-projected orthorhombic and face-centered orthorhombic (fco) BZs, respectively (see panels d-f). (b) The selected energies are shown on the measured band structure. (d) Orthorhombic unit cell of PdSe<sub>2</sub> with the corresponding BZ. The orange-shaded area sketches the surface-projected BZ (SBZ). (f) fco unit cell describing the Pd arrangement with the corresponding BZ and its surface projection (blue-shaded area). (e) Comparison of orthorhombic and fco SBZs.

paraboloids of the top-most VB. By comparing Fig.3a and Fig.3c, one can deduce that all  $\bar{\Gamma}$  points with Miller indices satisfying the relation  $h+k = \text{odd}$  are missing in panel c. Although surprising at first glance, this observation finds a straightforward rationale by assuming a different crystal symmetry.

We will unfold this concept referring to Fig.3d-f. Panel d recalls the orthorhombic unit cell of PdSe<sub>2</sub> and the corresponding BZ. It is known that ARPES measurements of solids probe the so-called surface-projected BZ (SBZ) based on energy and momentum conservation [29]. In panel d the SBZ is represented by the orange-shaded area. A closer inspection of the unit cell reveals that Pd atoms arrange on a *face-centered* orthorhombic (fco) lattice, as evident in panel f: if chalcogen atoms were absent, the corresponding first BZ would be the one sketched on the right-hand side [30] (notice the similarity with the BZ of the standard face-centered cubic lattice) [31]. Panel e compares the SBZs of the orthorhombic (panel d)

and the fcc (panel f) cells with identical lattice parameters. It can easily be verified that the following relations hold among wavevectors:  $\bar{\Gamma}\bar{X} = \pi/a$ ,  $\bar{\Gamma}\bar{Y} = \pi/b$ ,  $\bar{\Gamma}\bar{C} = 2\pi/a$ ,  $\bar{\Gamma}\bar{D} = 2\pi/b$ .

Returning to the photoemission map of Fig.3c, the blue dashed lines identify the SBZ of the fcc unit cell and each elliptical shape is centered at the  $\bar{\Gamma}$  point of the face-centered lattice. Since Pd atoms arrange on an fcc lattice, our ARPES analysis suggests that the top-most VB originates predominantly from Pd orbitals with little contribution from Se.

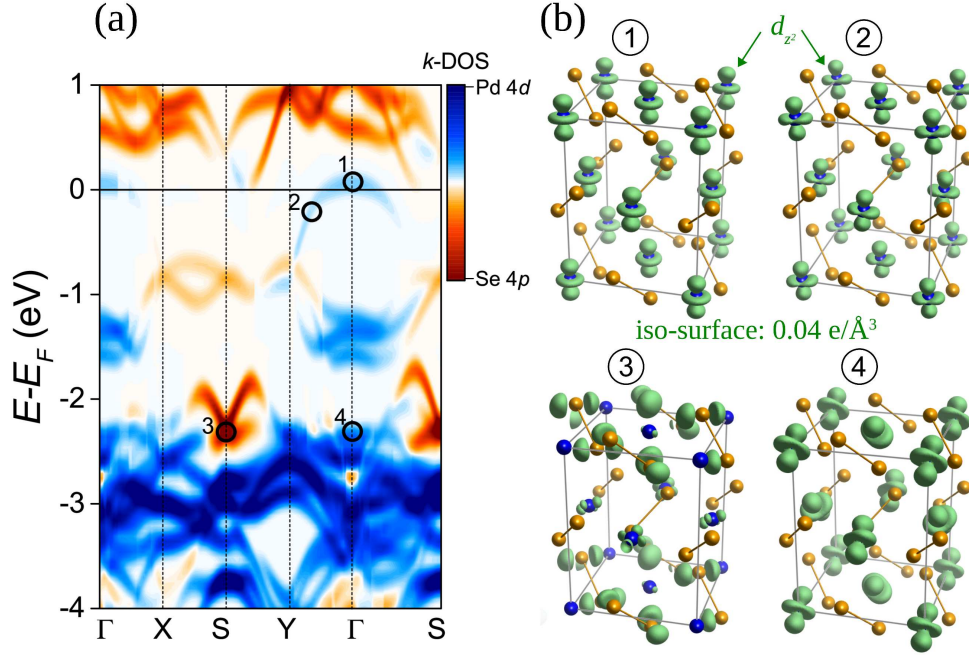


FIG. 4: (a) Difference between Pd 4d-projected and Se 4p-projected  $k$ -DOS. Blue and red colour represent Pd and Se character, respectively. (b) Electron density (iso-surface value at  $0.04 \text{ e}/\text{\AA}^3$ ) at the four selected points of the band structure labeled in panel a.

In order to support this hypothesis, we have computed the orbital-projected  $k$ -DOS and wave functions at selected points of the band structure. Fig.4a reports the *difference* between Pd 4d-projected and Se 4p-projected  $k$ -DOS along the same path of the reciprocal space employed previously in Fig.2 (see Methods for more details on Fig.4). Blue or red colour represents the dominant Pd or Se character, respectively. The highest VB shows a strong Pd 4d character with spectral weight  $\sim 3$  times larger than Se 4p and marginal contributions from other atomic orbitals. On the other hand, at  $E - E_F = -2.3 \text{ eV}$  (i.e. the same as Fig.3a), the dominant orbital character varies with the specific position on the BZ. Here, it is of interest to visualize the wave functions in real space: Fig.4b displays the electron

density at four representative points of the band structure, labeled by circles in panel a. The iso-surface value is taken at  $0.04 \text{ e}/\text{\AA}^3$ . On the highest VB (labels 1 and 2) the electron density is centered at Pd atoms with  $d_{z^2}$ -like symmetry. At  $E - E_F = -2.3 \text{ eV}$  (labels 3 and 4) the charge distribution depends on the position within the BZ: at the  $S$  point (label 3) it is dominated by Se  $4p$  orbitals [32], while at  $\Gamma$  (label 4) it is combination of Pd  $4d$  states. These results support our hypothesis that the same single orbital of Pd (i.e.  $4d_{z^2}$ ) shapes the top-most VB. Recalling that Pd atoms form an fcc lattice, this symmetry is retained also in reciprocal space, as revealed by our ARPES data (see Fig.3c). A simple tight binding approach leads to the same conclusion and is reported in the Methods section. At larger binding energies both Pd and Se orbitals contribute to the band structure, exhibiting the standard orthorhombic symmetry of Fig.3a.

In conclusion, we have measured the electronic band structure of bulk PdSe<sub>2</sub> by angle-resolved photoemission spectroscopy. Within the experimental accuracy, our data confirm its semiconducting nature with a minimum band gap of 50 meV (i.e. the instrumental resolution) since no evidence of conduction band across the Fermi level has been observed, while all electronic dispersive features below  $E_F$  are well-reproduced by our DFT calculations. Furthermore, we have demonstrated a remarkable sensitivity of the ARPES technique to site-specific symmetries of the electronic structure. This finding can be pivotal in tuning the electronic properties of PdSe<sub>2</sub>-based heterostructures [33], analogous to the observed dependence of the gap on the band character of MoS<sub>2</sub>/graphene [34, 35]. Moreover, we envisage that the chemical selectivity of ARPES allows a fine-tuning of the electronic properties. For example, chemical substitution of metal atoms [36] will give rise to specific changes in the VB related both to doping and to modifications in the surface symmetry, to which ARPES will be sensitive. We believe this implementation is not limited to PdSe<sub>2</sub>, but it applies to a much wider class of compounds with complex crystal structures and can help clarify the subtle interactions related to correlated electronic phases, such as metal-insulator transitions, charge density waves and superconductivity [37, 38].

### Acknowledgments

EC acknowledges funding from the Italian PRIN Grant 2017BZPKSZ. Some of the computational work was performed on the University of Bath's High Performance Computing Facility.

### Author Contributions

E.C. and C.J.S. proposed the experiments. M.C. performed the ARPES measurements. M.C., C.J.S and E.C. analysed the experimental data. D.W. and E.C. performed the DFT calculations. E.C. wrote the manuscript with input from all authors.

### Competing interests

The authors declare no competing interests.

## METHODS

**ARPES.** Bulk PdSe<sub>2</sub> crystals were obtained commercially from HQ Graphene [39]. Samples were cleaved in ultra-high vacuum ( $10^{-10}$  mbar) to expose a clean surface. Photoemission measurements were performed at the Spectromicroscopy beamline of the Elettra light source using 74 eV linearly polarized radiation focused to an approximately 0.6  $\mu\text{m}$  diameter spot by a Schwarzschild objective [40] and incident at 45° with respect to the sample. The energy and momentum resolution of the hemispherical electron analyzer are  $\sim 50$  meV and  $0.03 \text{ \AA}^{-1}$ , respectively. The sample temperature was maintained at 95 K.

**DFT.** The electronic band structure of PdSe<sub>2</sub> was computed with the Quantum Espresso package [41]. Exchange-correlation was considered using the Perdew-Burke-Ernzerhof functional revised for solids (PBEsol). Van der Waals interaction among PdSe<sub>2</sub> layers was included using the semiempirical Grimme’s DFT-D2 correction [42]. Atoms were allowed to relax until the residual forces were below  $0.0026 \text{ eV/\AA}$ . Cutoff energy of 60 Ry and  $8 \times 8 \times 6$   $k$ -point mesh were used. The iso-surface rendering in Fig.4b was performed with the VESTA software [43].

**Absence of CB evidence in ARPES data.** Fig.5 reports three constant-energy ARPES maps of PdSe<sub>2</sub> across the Fermi level ( $E - E_F = +0.5, 0, -0.5 \text{ eV}$ , top to bottom). Each map employs a logarithmic intensity scale ranging from 5% to 100% of the respective maximum. Even well above  $E_F$  we have detected no sign of electron pockets originating from the CB, as DFT calculation would predict. Although we are not able to determine the value of the band gap with static ARPES, our data uphold the semiconducting nature of bulk PdSe<sub>2</sub>.

**Orbital character of the band structure (Fig.4a).** Pd 4d and Se 4p electrons determine the valence and conduction states of PdSe<sub>2</sub>. It is instructive to "visualize" the specific orbital character and in particular the Pd-Se *duality* along high symmetry lines of the BZ. Here, we employ a simple colour-coded approach: the  $k$ -resolved density of states

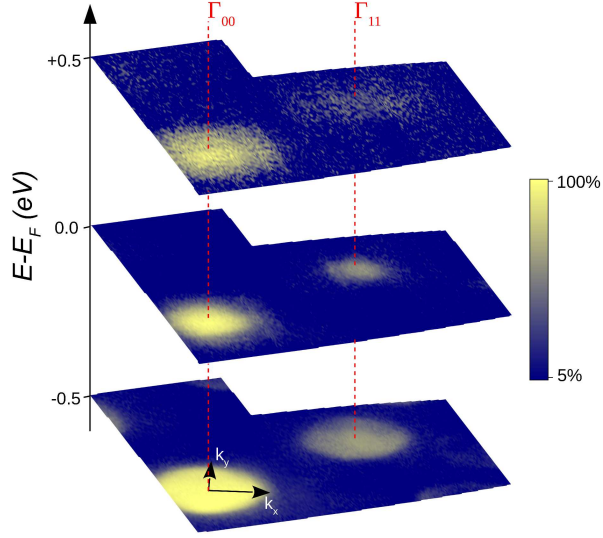


FIG. 5: ARPES constant energy maps at  $E - E_F = -0.5$  (bottom), 0 (middle) and  $+0.5$  eV (top), revealing no sign of the CB.

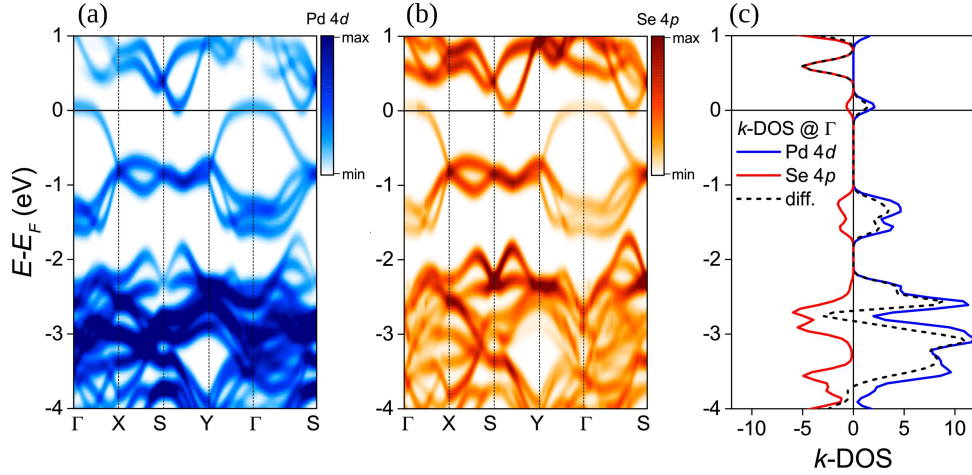


FIG. 6:  $k$ -DOS of (a) Pd 4d orbitals and (b) Se 4p orbitals. (c) Comparison of Pd 4d (blue) and Se 4p (red)  $k$ -DOS at the  $\Gamma$  point and their difference (black-dashed).

projected on Pd 4d and Se 4p are shown in Fig.6a and Fig.6b, respectively. Taking the difference between the data of these two graphs we obtain Fig.4a, where blue and red colours encode positive (Pd) and negative (Se) values. As an example, the Pd and Se  $k$ -DOS (the latter is represented on the negative abscissa) and their difference at the  $\Gamma$  point are shown in Fig.6c. Notice, in particular, that the Pd-projected  $k$ -DOS at the Fermi level (i.e. the VB top) is approximately 3 times larger than Se, as claimed in the main manuscript.

**Tight binding approach and matrix element effect.** In a regular  $\text{MX}_6$  octahedral complex ( $O_h$  symmetry) the five outer  $d$  orbitals of the transition metal M arrange into the high-energy, double-degenerate  $e_g$  and the low-energy, triple-degenerate  $t_{2g}$  states [44], as sketched in Fig.7a. A closer look at the crystal structure of  $\text{PdSe}_2$ , shown in Fig.7b, reveals

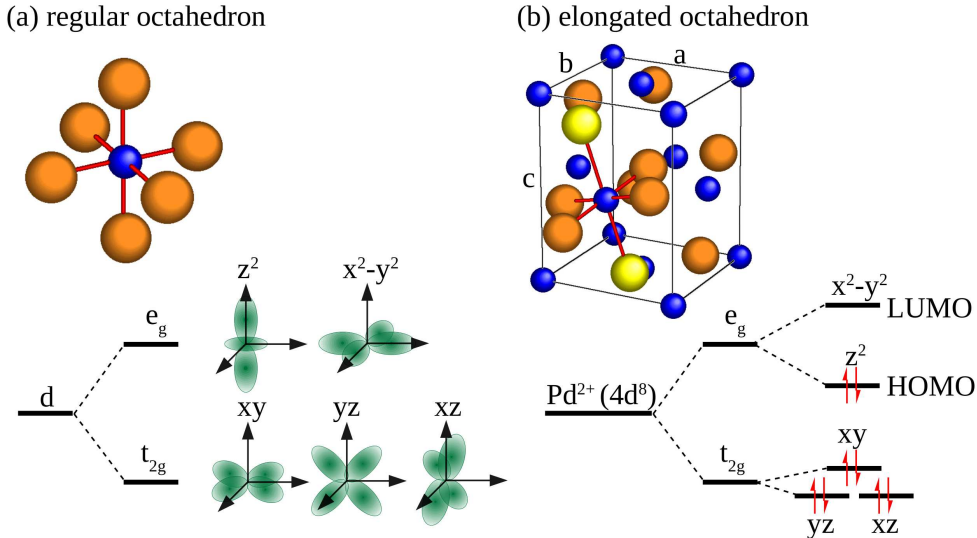


FIG. 7: (a) Regular  $\text{MX}_6$  octahedron with the corresponding crystal field splitting of  $d$  orbitals into  $e_g$  and  $t_{2g}$  states. (b) Elongated  $\text{PdSe}_6$  octahedron along the  $c$ -axis: the degenerate  $e_g$  states split into HOMO and LUMO.

that each Pd is surrounded by four Se atoms belonging to the same monolayer and two apical atoms (in yellow colour) belonging to the nearest upper and lower layers. The six chalcogen atoms form an octahedron elongated along the  $c$ -axis ( $D_{4h}$  symmetry). This distortion lifts the degeneracy of the  $e_g$  states, resulting in the  $d_{z^2}$  orbital being energetically more favorable than the  $d_{x^2-y^2}$  [44–46]. As we already pointed out, in  $\text{PdSe}_2$  the oxidation state of Pd is +2 and its electronic configuration is therefore  $4d^8$ : six of these electrons fill the  $t_{2g}$  states completely, while the remaining two occupy the  $d_{z^2}$  orbital, leaving  $d_{x^2-y^2}$  empty.  $d_{z^2}$  is therefore the highest occupied molecular orbital (HOMO) forging the top of the VB, while  $d_{x^2-y^2}$  represents the lowest unoccupied molecular orbital (LUMO) contributing the bottom of the CB, in agreement with our own calculations (Fig.4b) and other recent work [47].

We can now elucidate the symmetry features of the top-VB observed by photoemission using a simple 2D tight binding approach that involves only the HOMO. Metal atoms of a  $\text{PdSe}_2$  monolayer arrange on a rectangular lattice as shown in Fig.8. For simplicity we will

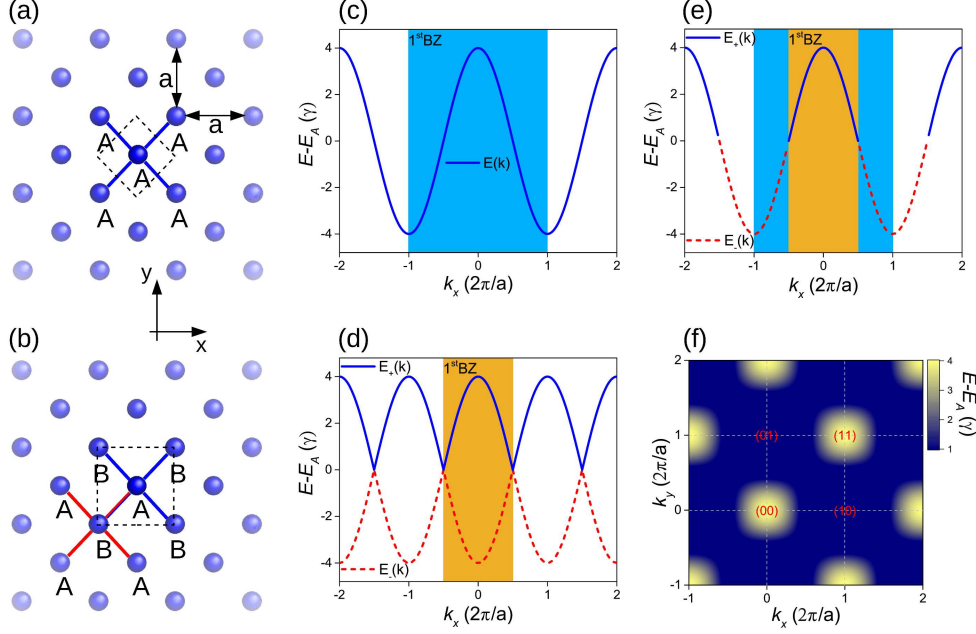


FIG. 8: Pd atoms of a single PdSe<sub>2</sub> layer using (a) the fcc unit cell, (b) the orthorhombic cell. Tight-binding VB dispersion employing (c) the fcc cell, (d) the orthorhombic cell. (e) Equivalence of (c) and (d) after considering matrix element effect. (f) Top-VB simulation on the  $xy$  reciprocal plane (compare with the experimental data of Fig.3c). The Miller indices refer to the orthorhombic cell: the missing VB peaks at (10) and (01) endorse the fcc symmetry.

assume a square lattice of side  $a$ . If the fcc unit cell is used (panel a), a single site  $A$  is sufficient to describe the crystal. On the other hand, if the orthorhombic unit cell is assumed (panel b) two sites  $A$  and  $B$  must be considered: each atom  $A(B)$  is surrounded by four nearest neighbors  $B(A)$ . In the fcc case, a tight binding approach is straightforward. Let  $|R_A\rangle$  be the Wannier wave function at the specific lattice site  $R$  (i.e. the  $d_{z^2}$  orbital). The overlap integral is  $\gamma = \langle R_A|U|0_A\rangle$  ( $U$  is the periodic lattice potential), where  $R$  runs over the 4 nearest neighbors  $(+a/2, +a/2)$ ,  $(+a/2, -a/2)$ ,  $(-a/2, +a/2)$ ,  $(-a/2, -a/2)$  and the eigenvalue of the hamiltonian  $\mathbb{H}$  is  $E(k) = E_A + \gamma \sum_{n.n.} e^{ikR} = E_A + 4\gamma \cos(k_x a/2) \cos(k_y a/2)$ , with  $E_A = \langle R_A|\mathbb{H}|R_A\rangle$ . Fig.8c shows the resulting VB dispersion along the  $x$ -axis ( $k_y = 0$ ). If the orthorhombic cell is used, two Wannier wave functions  $|R_A\rangle$  and  $|R_B\rangle$  form the basis of the tight binding hamiltonian:

$$\mathbb{H} = \begin{pmatrix} E_A & h \\ h^* & E_B \end{pmatrix} \quad (1)$$

It can easily be verified that the hopping term between sites  $A$  and  $B$  is  $h = 4\gamma \cos(k_x a/2) \cos(k_y a/2)$  like in the previous fco case. Since sites  $A$  and  $B$  are equivalent, it also follows that  $E_A = E_B$ . Thus, the two eigenvalues are  $E_{\pm}(k) = E_A \pm |4\gamma \cos(k_x a/2) \cos(k_y a/2)|$ . Fig.8d depicts  $E_{\pm}(k)$  along the  $x$ -axis ( $k_y = 0$ ). The corresponding eigenstates are  $(\pm \frac{h}{|h|}, 1)$  and the generic wave function at the lattice site  $R$  reads [48]:  $|R_{\pm}\rangle = \pm \frac{h}{|h|} e^{ikR_A} |R + R_A\rangle + e^{ikR_B} |R + R_B\rangle$ . In the free electron final state approximation (here, the final state  $|k_f\rangle$  is a plane wave with wavevector  $k_f$ ), the photoemission matrix element  $\mathbb{M}$  is expressed as the Fourier component of the tight binding orbital  $|0_{\pm}\rangle$  [48], i.e.

$$\mathbb{M} \propto \langle k_f | 0_{\pm} \rangle = \langle k_f | (\pm \frac{h}{|h|} e^{ikR_A} |R_A\rangle + e^{ikR_B} |R_B\rangle) \rangle \quad (2)$$

$$= \pm \frac{h}{|h|} e^{ikR_A} \langle k_f | R_A \rangle + e^{ikR_B} \langle k_f | R_B \rangle \quad (3)$$

$$= \pm \frac{h}{|h|} e^{i(k-k_f)R_A} \langle k_f | 0_A \rangle + e^{i(k-k_f)R_B} \langle k_f | 0_B \rangle \quad (4)$$

which, using the momentum conservation ( $k = k_f$ ), leads to the following photoemission intensity:

$$I_{\pm} \propto |\mathbb{M}|^2 \propto \left| \pm \frac{h}{|h|} \langle k_f | 0_A \rangle + \langle k_f | 0_B \rangle \right|^2 = |\langle k_f | 0_A \rangle|^2 + |\langle k_f | 0_B \rangle|^2 \pm \frac{h}{|h|} 2\Re(\langle k_f | 0_A \rangle \langle 0_B | k_f \rangle) \quad (5)$$

that simplifies to  $I_{\pm} \propto 2 |\langle k_f | 0_A \rangle|^2 \left(1 \pm \frac{h}{|h|}\right)$  since  $|0_A\rangle = |0_B\rangle$ . At this point we notice that  $\frac{h}{|h|} = \text{sgn}[\cos(k_x a/2) \cos(k_y a/2)]$ . Thus,  $I_{\pm} \propto (1 \pm \text{sgn}[\cos(k_x a/2) \cos(k_y a/2)])$ . Referring to Fig.8d, it is easily verified that the previous equation completely suppresses the photoemission intensity of one eigenvalue  $E_{\pm}(k)$  depending on the values of  $k_x$  and  $k_y$ . Fig.8e-f show the results: as expected, the fco band structure of Fig.8c and the experimental data of Fig.3c are recovered since the use of two equivalent sites is redundant and the appropriate unit cell is the fco.

- 
- [1] S. Manzeli, D. Ovchinnikov, D. Pasquier, O. V. Yazyev, A. Kis, 2D transition metal dichalcogenides. *Nat. Rev. Mater.* **2**, 17033 (2017).
- [2] K. F. Mak, J. Shan, Photonics and optoelectronics of 2D semiconductor transition metal dichalcogenides. *Nat. Photonics* **10**, 216-226 (2016).
- [3] A. D. Oyedele *et al.*, PdSe<sub>2</sub>: Pentagonal Two-Dimensional Layers with High Air Stability for Electronics. *J. Am. Chem. Soc.* **139**, 14090-14097 (2017).
- [4] P. Miró, M. Ghorbani-Asl, T. Heine, Two Dimensional Materials Beyond MoS<sub>2</sub>: Noble Transition-Metal Dichalcogenides. *Angew. Chem. Int. Ed.* **53**, 3015 (2014).
- [5] Y. Wang, L. Li, W. Yao, S. Song, J. T. Sun, J. Pan, X. Ren, C. Li, E. Okunishi, Y.-Q. Wang, et al., Monolayer PtSe<sub>2</sub>, a New Semiconducting Transition-Metal-Dichalcogenide, Epitaxially Grown by Direct Selenization of Pt. *Nano Lett.* **15**, 401 (2015).
- [6] A. Ciarrocchi, A. Avsar, D. Ovchinnikov, A. Kis, Thickness-modulated metal-to-semiconductor transformation in a transition metal dichalcogenide. *Nat. Commun.* **9**, 919 (2018).
- [7] F. Xia, H. Wang, Y. Jia, Rediscovering black phosphorus as an anisotropic layered material for optoelectronics and electronics. *Nat. Commun.* **5**, 4458 (2014).
- [8] P. Chen, N. Li, X. Chen, W.-J. Ong, and X. Zhao, The rising star of 2D black phosphorus beyond graphene: synthesis, properties and electronic applications. *2D Mater.* **5**, 014002 (2018).
- [9] R. Gusmao, Z. Sofer, M. Pumera, Black Phosphorus Rediscovered: From Bulk Material to Monolayers. *Angew. Chem. Int. Ed.* **56**, 8052 (2017).
- [10] H. Hedayat, A. Ceraso, G. Soavi, S. Akhavan, A. Cadore, C. Dallera, G. Cerullo, A. C. Ferrari, E. Carpene, Non-equilibrium band broadening, gap renormalization and band inversion in black phosphorus. *2D Mater.* **8**, 025020 (2021).
- [11] V. Tran, R. Soklaski, Y. Liang, L. Yang, Layer-controlled band gap and anisotropic excitons in few-layer black phosphorus. *Phys. Rev. B* **89**, 235319 (2014).
- [12] J. Yu, X. Kuang, J. Li, J. Zhong, C. Zeng, L. Cao, Z. Liu, Z. Zeng, Z. Luo, T. He, A. Pan, Y. Liu, Giant nonlinear optical activity in two-dimensional palladium diselenide. *Nat. Comm.* **12**, 1083 (2021).

- [13] A. Di Bartolomeo, A. Pelella, X. Liu, F. Miao, M. Passacantando, F. Giubileo, A. Grillo, L. Iemmo, F. Urban, S.-J. Liang, Pressure-Tunable Ambipolar Conduction and Hysteresis in Thin Palladium Diselenide Field Effect Transistors. *Adv. Funct. Mater.* **29**, 1902483 (2019).
- [14] S. Deng, L. Li, Y. Zhang, ACS Appl. Strain Modulated Electronic, Mechanical, and Optical Properties of the Monolayer PdS<sub>2</sub>, PdSe<sub>2</sub> and PtSe<sub>2</sub> for Tunable Devices. *Nano Mater.* **1**, 1932-1939 (2018).
- [15] W. Luo, A. D. Oyedele, Y. Gu, T. Li, X. Wang, A. V. Haglund, D. Mandrus, A. A. Puretzky, K. Xiao, L. Liang, X. Ling, Anisotropic Phonon Response of Few-Layer PdSe<sub>2</sub> under Uniaxial Strain. *Adv. Funct. Mater.* **30**, 2003215 (2020).
- [16] L.-H. Zeng, D. Wu, S.-H. Lin, C. Xie, H.-Y. Yuan, W. Lu, S. P. Lau, Y. Chai, L.-B. Luo, Z.-J. Li, Y. H. Tsang, Controlled Synthesis of 2D Palladium Diselenide for Sensitive Photodetector Applications. *Adv. Funct. Mater.* **29**, 1806878 (2019).
- [17] M. Sun, J.-P. Chou, L. Shi, J. Gao, A. Hu, W. Tang, G. Zhang, Few-Layer PdSe<sub>2</sub> Sheets: Promising Thermoelectric Materials Driven by High Valley Convergence. *ACS Omega* **3**, 5971-5979 (2018).
- [18] L. Pi, L. Li, K. Liu, Q. Zhang, H. Li, T. Zhai, Recent Progress on 2D Noble-Transition-Metal Dichalcogenides. *Adv. Funct. Mater.* **29**, 1904932 (2019).
- [19] A. Hassan, Y. Guo, Q. Wang, Performance of the Pentagonal PdSe<sub>2</sub> Sheet as a Channel Material in Contact with Metal Surfaces and Graphene. *ACS Appl. Electron. Mater.* **2**, 2535 (2020).
- [20] Y.-S. Lan, X.-R. Chen, C.-E. Hu, Y. Cheng, Q.-F. Chen, Penta-PdX<sub>2</sub> (X = S, Se, Te) monolayers: promising anisotropic thermoelectric materials. *J. Mater. Chem. A* **7**, 11134 (2019).
- [21] R. Grønvold, E. Røst, The crystal structure of PdSe<sub>2</sub> and PdS<sub>2</sub>. *Acta Cryst.* **10**, 329 (1957).
- [22] R. Kempt, A. Kuc, T. Heine, Two-Dimensional Noble-Metal Chalcogenides and Phosphochalcogenides. *Angew. Chem. Int. Ed.* **59**, 9242 (2020).
- [23] L.-S. Lu et al., Layer-Dependent and In-Plane Anisotropic Properties of Low-Temperature Synthesized Few-Layer PdSe<sub>2</sub> Single Crystals. *ACS Nano*, **14**, 4963-4972 (2020).
- [24] G. Zhang, M. Amani, A. Chaturvedi, C. Tan, J. Bullock, X. Song, H. Kim, D.-H. Lien, M. C. Scott, H. Zhang, A. Javey, Optical and electrical properties of two-dimensional palladium diselenide. *Appl. Phys. Lett.* **114**, 253102 (2019).
- [25] W. Lei, B. Cai, H. Zhou, G. Heymann, X. Tang, S. Zhang, X. Ming, Ferroelastic lattice

- rotation and band-gap engineering in quasi 2D layered-structure PdSe<sub>2</sub> under uniaxial stress. *Nanoscale* **11**, 12317-12325 (2019)
- [26] A. Hamidani, B. Bennecer, K. Zanat, Structural and electronic properties of the pseudo-binary compounds PdX<sub>2</sub> (X = P, S and Se). *J. Phys. Chem. Solids* **71**, 42-46 (2010).
- [27] J. P. Perdew, Density functional theory and the band gap problem. *Int. J. Quantum Chemistry* **28**, 497-523 (1985).
- [28] J. P. Perdew, W. Yang, K. Burke, Z. Yang, E. K. U. Gross, M. Scheffler, G. E. Scuseria, T. M. Henderson, I. Ying Zhang, A. Ruzsinszky, H. Peng, J. Sun, E. Trushin, and A. Görling, Understanding band gaps of solids in generalized Kohn-Sham theory. *PNAS* **114**, 2801-2806 (2017).
- [29] S. Hüfner, *Photoelectron Spectroscopy* (Springer, Berlin, 2003).
- [30] W. Setyawan, S. Curtarolo, High-throughput electronic band structure calculations: Challenges and tools. *Computational Materials Science* **49**, 299-312 (2010).
- [31] N. W. Ashcroft and N.D. Mermin, *Solid State Physics* (Saunders College, Philadelphia, USA 1976).
- [32] Point 3 in Fig.4a is four-fold degenerate. Here we show the iso-surface of one of the bands, the others differing only by 4p orbital orientation and/or Se atom.
- [33] E. Li, D. Wang, P. Fan, R. Zhang, Y.-Y. Zhang, G. Li, J. Mao, Y. Wang, X. Lin, S. Du, H.-J. Gao, Construction of bilayer PdSe<sub>2</sub> on epitaxial graphene. *Nano Research* **11**, 5858-5865 (2018).
- [34] H. C. Diaz, J. Avila, C. Chen, R. Addou, M. C. Asensio, M. Batzill, Direct Observation of Interlayer Hybridization and Dirac Relativistic Carriers in Graphene/MoS<sub>2</sub> van der Waals Heterostructures. *Nano Lett.* **15**, 1135-1140 (2015).
- [35] D. Pierucci, H. Henck, J. Avila, A. Balan, C. H. Naylor, G. Patriarache, Y. J. Dappe, M. G. Silly, F. Sirotti, A. T. C. Johnson, M. C. Asensio, A. Ouerghi, Band Alignment and Minigaps in Monolayer MoS<sub>2</sub>-Graphene van der Waals Heterostructures. *Nano Lett.* **16**, 4054-4061 (2016).
- [36] J. Gao, Y. D. Kim, L. Liang, J. C. Idrobo, P. Chow, J. Tan, B. Li, L. Li, B. G. Sumpter, T.-M. Lu, V. Meunier, J. Hone, N. Koratkar, Transition-Metal Substitution Doping in Synthetic Atomically Thin Semiconductors. *Adv. Mater.* **28**, 9735-9743 (2016).
- [37] H. Hedayat, C. J. Sayers, D. Bugini, C. Dallera, D. Wolverson, T. Batten, S. Karbassi, S. Friedemann, G. Cerullo, J. van Wezel, S. R. Clark, E. Carpene, E. Da Como, Excitonic and

- lattice contributions to the charge density wave in  $1T$ -TiSe<sub>2</sub> revealed by a phonon bottleneck. Phys. Rev. Research **1**, 023029 (2019).
- [38] C. J. Sayers, H. Hedayat, A. Ceraso, F. Museur, M. Cattelan, L. S. Hart, L. S. Farrar, S. Dal Conte, G. Cerullo, C. Dallera, E. Da Como, E. Carpene, Coherent phonons and the interplay between charge density wave and Mott phases in  $1T$ -TaSe<sub>2</sub>. Phys. Rev. B **102**, 161105(R) (2020).
- [39] <http://www.hqgraphene.com>
- [40] P. Dudin, P. Lacovig, C. Fava, E. Nicolini, A. Bianco, G. Cauetero, A. Barinov, Angle-resolved photoemission spectroscopy and imaging with a submicrometre probe at the SPECTROMICROSCOPY-3.2L beamline of Elettra. Journal of Synchrotron Radiation **17**, 445-450 (2010).
- [41] P. Giannozzi *et al.*, Advanced capabilities for materials modelling with Quantum ESPRESSO. J. Phys.: Condens. Matter **29**, 465901 (2017).
- [42] S. Grimme, J. Antony, S. Ehrlich, and H. Krieg, A consistent and accurate ab initio parametrization of density functional dispersion correction (DFT-D) for the 94 elements H-Pu. J. Chem. Phys. **132**, 154104 (2010).
- [43] K. Momma and F. Izumi, VESTA 3 for three-dimensional visualization of crystal, volumetric and morphology data. J. Appl. Crystallogr. **44**, 1272-1276 (2011).
- [44] I. B. Bersuker, *Electronic structure and properties of transition metal compounds: introduction to the theory* (John Wiley and Sons, Hoboken, New Jersey, USA, 2010).
- [45] If ligands with apical atoms are negligible,  $d$  orbitals split into the square planar coordination where  $d_{xy}$  has higher energy than  $d_{z^2}$  (and the former becomes the HOMO), see Ref.[44].
- [46] C. Souldard, X. Rocquefelte, P.-E. Petit, M. Evain, S. Jobic, J.-P. Itié, P. Munsch, H.-J. Koo, and M.-H. Whangbo, Experimental and Theoretical Investigation on the Relative Stability of the PdS<sub>2</sub>- and Pyrite-Type Structures of PdSe<sub>2</sub>. Inorg. Chem. **43**, 1943 (2004).
- [47] W. Lei, W. Wang, X. Ming, S. Zhang, G. Tang, X. Zheng, H. Li, C. Autieri, Structural transition, metallization, and superconductivity in quasi-two dimensional layered PdS<sub>2</sub> under compression. Phys. Rev. B **101**, 205149 (2020).
- [48] S. Moser, An experimentalist's guide to the matrix element in angle resolved photoemission. Journal of Electron Spectroscopy and Related Phenomena **214**, 29-52 (2017).